



Tailoring the Physical Properties of (Bi, Pb)-2212 Superconductor by the Addition of Cd_{0.95}Mn_{0.05}O Nanoparticles

S. Abbas¹ · H. Basma² · R. Awad^{1,2} · M. Matar²

Received: 4 February 2022 / Accepted: 17 May 2022 / Published online: 15 June 2022
© The Author(s), under exclusive licence to Springer Science+Business Media, LLC, part of Springer Nature 2022

Abstract

The effect of CdMnO addition on the physical properties of Bi-2212 superconductors was investigated. The conventional solid-state reaction technique was employed for the synthesis of $(\text{Cd}_{0.95}\text{Mn}_{0.05}\text{O})_x \text{Bi}_{1.6} \text{Pb}_{0.4} \text{Sr}_{1.9} \text{Ca}_{1.1} \text{Cu}_{2.1} \text{O}_{8+\delta}$ samples with $0.00 \leq x \leq 0.10$ wt.%. The X-ray diffraction confirms the formation of the orthorhombic phase of Bi-2212 superconductors. The lattice parameter a shows an increase with x , conversely the lattice parameters b and c show a decrease. The scanning electron microscope (SEM) images have shown an enhancement in the grain connectivity and a reduction of voids due to the CdMnO addition. The Fourier transform infrared (FTIR) spectroscopy analysis shows a remarkable shift in the wave number positions due to the addition of CdMnO nanoparticles. The superconducting transition temperature (T_c) and the critical current density (J_c) show an enhancement with CdMnO addition up to $x=0.05$ wt.%. The elemental composition and oxidation state of all elements were determined from the X-ray photoelectron emission (XPS) analysis. The work suggests a correlation between the variations of the superconducting properties and the dynamics of the cationic equilibrium reactions among Pb^{2+} ions in Bi^{3+} or Cu^{2+} sites. These equilibrium reactions are induced by the variations in the oxygen content produced by the addition of CdMnO nanoparticles.

Keywords Bi-2212 superconductor · CdMnO nanoparticles · FTIR · XPS · Resistivity

✉ H. Basma
h.basma@bau.edu.lb

¹ Department of Physics, Faculty of Science, Beirut Arab University, Beirut, Lebanon

² Department of Physics, Faculty of Science, Alexandria University, Alexandria 21511, Egypt

1 Introduction

Bi-based high-temperature superconductors (HTSC's) have been exploited in numerous technological and industrial applications [1, 2]. Owing to their noticeable lower power losses, high current and magnetic field carrying capacity [3], enhanced thermodynamic stability, and minimal weak link problems [4]. In addition to the previously mentioned favorable properties common to all binary Bi-based family, the (Bi,Pb)-2212 in specific is stable for a wide range of processing temperatures and possess high critical current density [5, 6], making its synthesis relatively simple and encouraging.

Since the discovery of the Bi-based superconductor ceramics, researchers have aimed to improve the Bi-based superconductor ceramics structural and superconducting properties, including crystal structure quality, superconducting flux pinning mechanism, and grain boundary linkage problems. The technique of the addition of nanoparticles [7–10] has proven to be very effective in this context. Gündoğmuş et al. [11] have reported the effect of the addition of Y_2O_3 nanoparticles on the Bi-2212 superconductor. The maximum values of the critical current density, J_c , and superconductivity transition temperature, T_c , were observed after the addition of 0.7% Y_2O_3 nanoparticles, without any alteration of the crystallographic structure. The influence of $SrZrO_3$ nanoparticles' addition on the microstructure of $Bi_2Sr_2CaCu_2O_{8+\delta}$ films was investigated by Zhang et.al [12]. The presence of flux pinning centers in the form of lattice distortions, shear stresses, and stacking faults was detected in the Bi-2212 matrix. It was believed that the enhanced performance of these superconducting films was a consequence of the pinning centers. The effect of substitution of Ca by Y in $Bi_2Sr_2Ca_{1-x}Y_xCu_2O_y$ superconducting samples was investigated [13]. T_c was enhanced up to 104 K for the sample $Bi_2Sr_2Ca_{0.7}Y_{0.3}Cu_2O_y$. This enhancement was attributed to the reduction of the supercurrent flow in the Bi-2212 system.

Transition doped CdO nanoparticles synthesized as nanoparticles or thin films have recently grabbed the attention of research groups [14–17]. It was reported that the transition metal doping enhances the structural, optical, and changes the magnetic signature of the host CdO matrix, allowing for exotic applications. In particular, much research was dedicated to Mn^{2+} doped CdO nanoparticles [18–20]. In this piece of research, we present, for the first time, the effect of the addition of CdMnO nanoparticles on the structural, vibrational, and superconducting properties of (Bi,Pb)-2212. We aim by this addition to enhance the physical properties of the superconducting samples that may pave the way for new applications.

2 Experimental Techniques

2.1 Preparation of $\text{Cd}_{0.95}\text{Mn}_{0.05}\text{O}$ Nanoparticles

$\text{Cd}_{0.95}\text{Mn}_{0.05}\text{O}$ nanoparticles were prepared by the following procedure: 24.64 g of CdCl_2 were dissolved in 50 ml of distilled water mixed with 0.35 g of MnCl_2 that was dissolved in 6.8 ml of distilled water. Then the sample was stirred with 2.9 g of EDTA for 30 min using a magnetic stirrer to reduce agglomeration. Afterward, the titration method was performed with the obtained solution using 2 M NaOH ($m=8$ g) until $\text{pH}=12$ then was heated for 2 h at $T=80$ °C during stirring. Next, the sample undergoes filtration method by using distilled water to remove impurities and spectator ions. Then it was dried for 16 h using the furnace to evaporate excess water, then crushed with a mortar. Finally, the calcination method was performed at $T=650$ °C for 3 h.

2.2 Preparation of $(\text{Cd}_{0.95}\text{Mn}_{0.05}\text{O})_x \text{Bi}_{1.6} \text{Pb}_{0.4} \text{Sr}_{1.9} \text{Ca}_{1.1} \text{Cu}_{2.1} \text{O}_8$ Samples

The standard solid-state reaction technique was applied for the preparation of superconducting: $(\text{Cd}_{0.95}\text{Mn}_{0.05}\text{O})_x \text{Bi}_{1.6} \text{Pb}_{0.4} \text{Sr}_{1.9} \text{Ca}_{1.1} \text{Cu}_{2.1} \text{O}_8$ samples with $x=0, 0.01, 0.02, 0.05$ and 0.1 wt %. The amounts of Bi_2O_3 , SrCO_3 , CaO , and CuO (Sigma-Aldrich with >99% purity) were mixed in stoichiometric ratios, ground, and sieved using a 53 μm sieve until a homogenous gray color mixture was obtained and the whole process was repeated once more to ensure a perfect mixing. The soft powders have been then placed in ceramic crucibles and put in a Nabertherm muffle furnace wherein they were heat-treated at 800 °C for 10 h, 820 °C for 20 h, and 830 °C for 40 h, with intermediate grinding and sieving. After that the pressing of the powder into a pellet is done using a SPECAC guide hydraulic press at 0.96 GPa and heated at 840 °C for 50 h with a cooling rate of 4 °C/min. The $(\text{Cd}_{0.95}\text{Mn}_{0.05}\text{O})$ nanoparticles, prepared by the co-precipitation method, were added finally after the pellet was ground again, and the mixture which was pressed and sintered again with a rate of 4 °C/min at 840 °C for 48 h and then cooled at a rate of 2 °C/min.

2.3 Sample Characterization

The X-ray powder diffraction characterization was performed using a Bruker D8 focus diffractometer with Cu K_α radiation ($\lambda=1.5406$ Å), with 2θ ranging from 20° to 60°, setting the voltage and the current at 40 kV and 40 mA, respectively. The morphology of the samples was investigated with the aid of the SEM technique using an SDD Apollo X with an accelerating voltage of 20 kV. The apparatus is equipped with an AIS 2100C microscope that operates at 20 kV up to an image resolution of 10 μm . Idiometric titration using potassium iodide (KI) in a two-step redox titration is used to determine the oxygen content of the samples. The detection of the endpoint of titration was done by using Potassium thiocyanate (KCSN). The functional groups were examined by performing Fourier transform infrared spectroscopy

(FTIR) with a Nicolet iS5 spectrometer on the samples mixed with KBr and pressed in disk shapes. The resistivity curves were obtained by employing the four-probe method. The Keithley 6221 digital nanometer was used to supply a steady current of 1 mA while the Keithley 181 digital nanometer was used to measure the voltage drop across the sample. With the aid of helium gas through a cryogenic duplex system, the refrigeration of the samples was done. The critical current density J_c of the samples was measured by the same conventional four-probe method used in electrical resistivity measurement. Here the voltage is a function of the applied current at a temperature of about 60 K using the same cooling system as in the resistivity measurement. The measuring technique was done as follows: the samples were glued to the holder with a very thin piece of thermal conducting paper soaked with a thin layer of thermal glue between them. The sample current was supplied by a homemade current source ($I_{\max} = 8$ A) and the voltage across the sample was measured by the digital nanometer Keithley 181. The average value of voltage is measured when the current is in the normal and reverse directions.

The KRATOS X SAM 800 spectrometer was used to perform X-ray photoelectron spectroscopy (XPS) experiments. The spectrometer uses a monochromatized Mg K α X-ray source that provides an X-ray spot with a diameter of 600 μm and a resolution of 0.7.

3 Results and Discussion

The room temperature XRD Patterns of the prepared samples: $(\text{Cd}_{0.95}\text{Mn}_{0.05}\text{O})_x \text{Bi}_{1.6}\text{Pb}_{0.4}\text{Sr}_{1.9}\text{Ca}_{1.1}\text{Cu}_{2.1}\text{O}_{8+\delta}$ ($x = 0.00, 0.01, 0.02, 0.05, \text{ and } 0.10$ wt.%), denoted by (Mn-0, Mn-1, Mn-2, Mn-4, and Mn-5, respectively), are displayed in Fig. 1.

The presence of the characteristic peaks between 20° and 60° confirmed the formation of the orthorhombic structure of Bi-2212 space by comparing with the ICDD entry N.00-082-2278 [21]. All XRD spectra demonstrate a single phased Bi-2212 with minor peaks of low intensity corresponding to the Bi-2201 phase. It is believed that the improved crystallinity and purity are attributed to the heat treatment, in specific the prolonged calcination at $T = 840^\circ\text{C}$ [22]. Moreover, peaks corresponding to the CdMnO phase were not detected probably because of its low concentration. There is no shift of the (2θ) position of the peaks with CdMnO addition, assuring the absence of chemical interaction between the Bi-2212 and CdMnO phases and hence the successful addition of CdMnO nanoparticles.

The lattice parameters a , b and c were determined by using a Reitveld refinement on the XRD patterns using the MAUD software [23]. The values of a , b and c are listed in Table 1.

The values of a show a slight increase with the CdMnO content, while the lattice parameters b and c decrease with the addition of CdMnO. The existence of the metal oxide nanoparticle (CdMnO) within the Bi2212 phase unit cell may create extra oxygen ions in the BiO layer. This excess oxygen content might induce the relocation of holes from the charge reservoir (BiO layer) to the Cu–O conducting plane [24, 25]. The effect of oxygen content is also reflected on the ratio c/a and the orthorhombic distortion OD (b/aa) which are calculated and

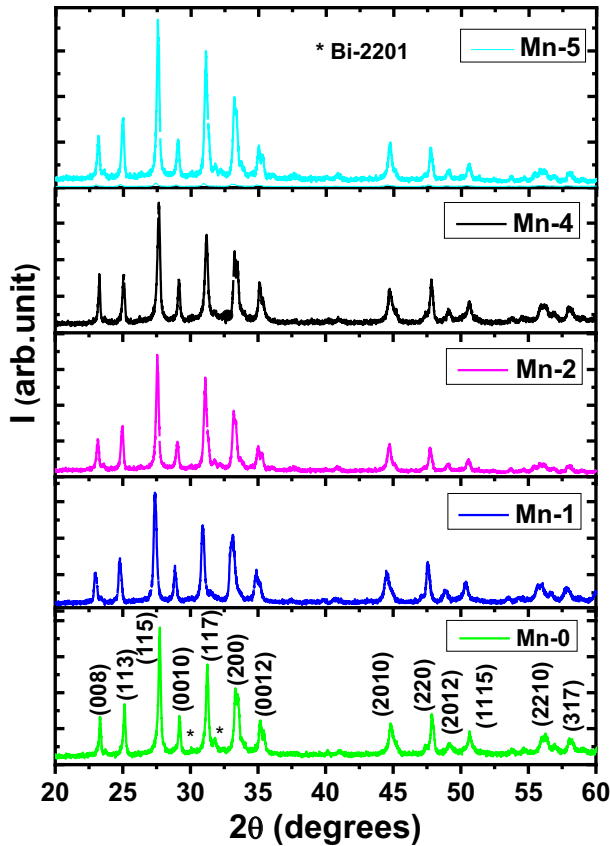


Fig. 1 XRD patterns of the (Bi,Pb)-2212 samples for various CdMnO nanoparticle additions. (Colour figure online)

Table 1 XRD parameters and orthorhombic distortion of (Bi,Pb)-2212 samples for various CdMnO nanoparticle additions

Parameter	Mn-0	Mn-1	Mn-2	Mn-4	Mn-5
a (Å)	5.416	5.417	5.417	5.418	5.419
b (Å)	5.388	5.384	5.381	5.374	5.373
c (Å)	30.861	30.842	30.840	30.821	30.804
c/a	5.698	5.693	5.693	5.688	5.6844
OD ($\times 10^{-2}$)	0.519	0.612	0.669	0.818	0.856

presented in Table 1. A reduction of c/a values with the addition of CdMnO nanoparticles is observed. The ratio c/a is strongly dependent on the oxygen content of the Bi-2212 superconducting phase. In particular, the excessive oxygen content within the BiO layers and the Cu–O bonding in the Cu–O planes [26–28]. The high oxygen content induces a Jahn–Teller distortion around the Cu^{2+} ion, leading to a reduction of the c/a ratio. An increase of OD is demonstrated with the

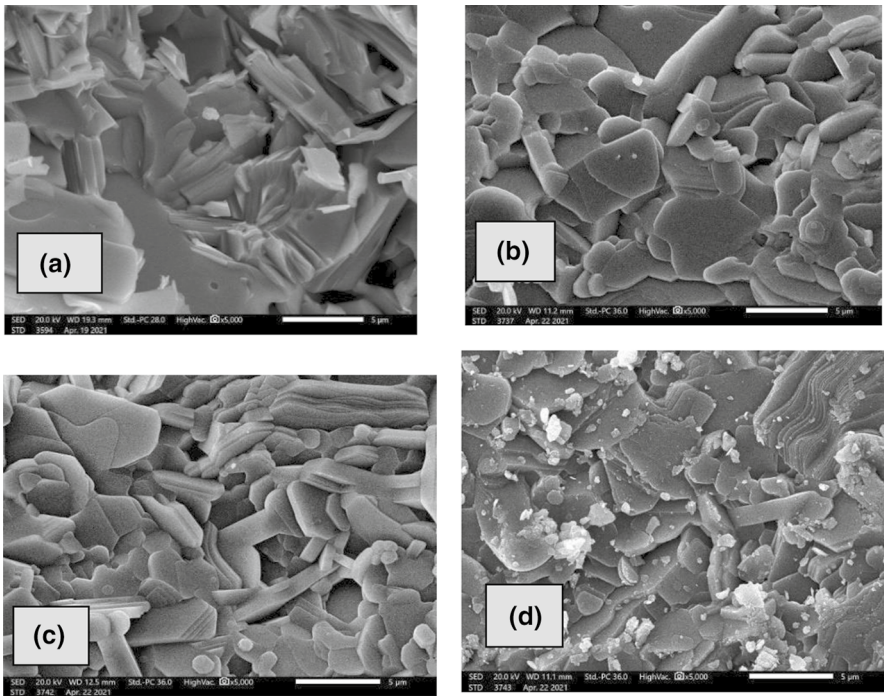


Fig. 2 SEM images of CdMnO nanoparticles-added (Bi,Pb)-2212 samples, **a** pure, **b** 0.02 wt%, **c** 0.05 wt%, **d** 0.10 wt%

addition of CdMnO. But, all values of OD are less than 1% approving the stability of the Bi, Pb-2212 phase [29].

Figure 2. depicts the SEM microscopy images of the (Bi, Pb)-2212 superconductor with different concentrations of CdMnO nanoparticles additions. The microstructures of the pure sample show large plate-like grains distributed randomly. As it is evident, that the increase in the concentration of CdMnO nanoparticles added for samples causes an enhancement in the growth of the grains, with the formation of a few platelet-like grains, as in (0.05 and 0.10) samples, and the formation also of flower-like grains, as in 0.10 sample. This enhancement might be due to the occupation of the added CdMnO nanoparticles of the grain boundary locations [30]. This is supported by the appearance of fine inclusions among the (Bi,Pb)-2212 grains. These inclusions correspond to the added nano CdMnO. This causes an enhancement of grain connectivity and a reduction of voids and cracks.

The oxygen content “y” determined from Idiometric titration analysis show an increase from 8.0875 for the pure sample to 8.2068, 8.3079, with the addition of $(\text{Cd}_{0.95}\text{Mn}_{0.05}\text{O})_x - (\text{Bi,Pb-2212})$ for $x=0.02$ and 0.10 wt.% samples, respectively. The increase in the oxygen content is compatible with the variation of the lattice parameters discussed in the XRD section. The effective valence of the Cu ions (Cu^{eff}) is calculated by applying electric equilibrium between the valence states of

the cations and anions as shown in Eq. 1 [31], assuming the valence of the elements as (Bi^{3+} , Pb^{2+} , Sr^{2+} , Ca^{2+} , Cd^{2+} , and O^{2-}):

$$\text{Cu}^{\text{eff}} = \frac{2y - [11.7 + 2x]}{2} \quad (1)$$

where x and y represent the Cd and O contents, respectively.

The values obtained for Cu^{eff} are 2.2375, 2.3368, and 2.3579 for the samples Mn-0, Mn-2, and Mn-5, respectively. The increase in Cu^{eff} is indispensable for the creation of the Bi-2212 phase. Studies have shown that the high T_c cuprates require the presence of Cu^{3+} ions in the form of excess oxygen in/or near the CuO_2 planes [32–36]. The effect of Cu valency and oxygen content will be reflected in the discussion of the Resistivity and XPS measurements analysis in the next sections.

The FTIR transmittance spectra plots in the wave number range ($400\text{--}4000\text{ cm}^{-1}$) of samples $(\text{CdMnO})_x(\text{Bi,Pb})\text{-2212}$ with $x=0, 0.01, 0.02, 0.05$ and 0.10 wt.% after calcination at $T=840\text{ }^\circ\text{C}$ are presented in Fig. 3. The absorption spectra with deconvolution plots are shown in Fig. 4 in the range $400\text{--}2000\text{ cm}^{-1}$, for a detailed characterization of the functional groups. The characterized absorbance peaks are associated with corresponding functional groups and are depicted in Table 2.

In all spectra, absorption peaks detected in the range ($3425.85\text{--}3434.92\text{ cm}^{-1}$) are associated with the stretching vibration of the intermolecular hydrogen

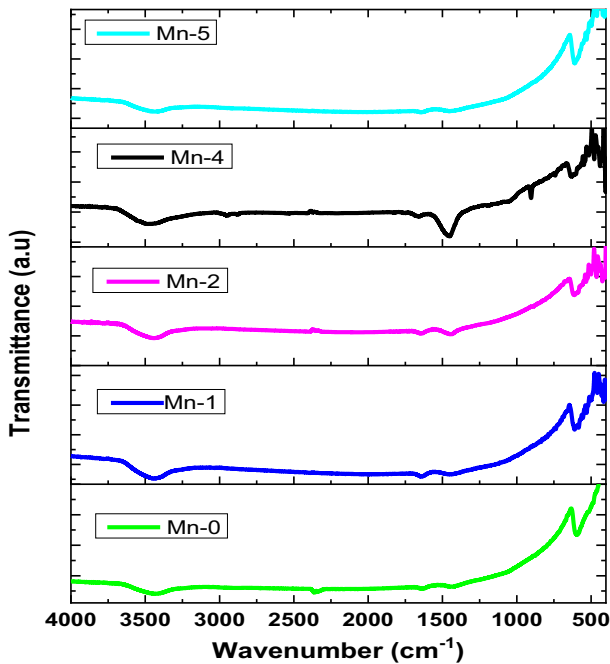


Fig. 3 FTIR Transmittance spectra of (Bi,Pb)-2212 samples for various CdMnO nanoparticle additions. (Colour figure online)

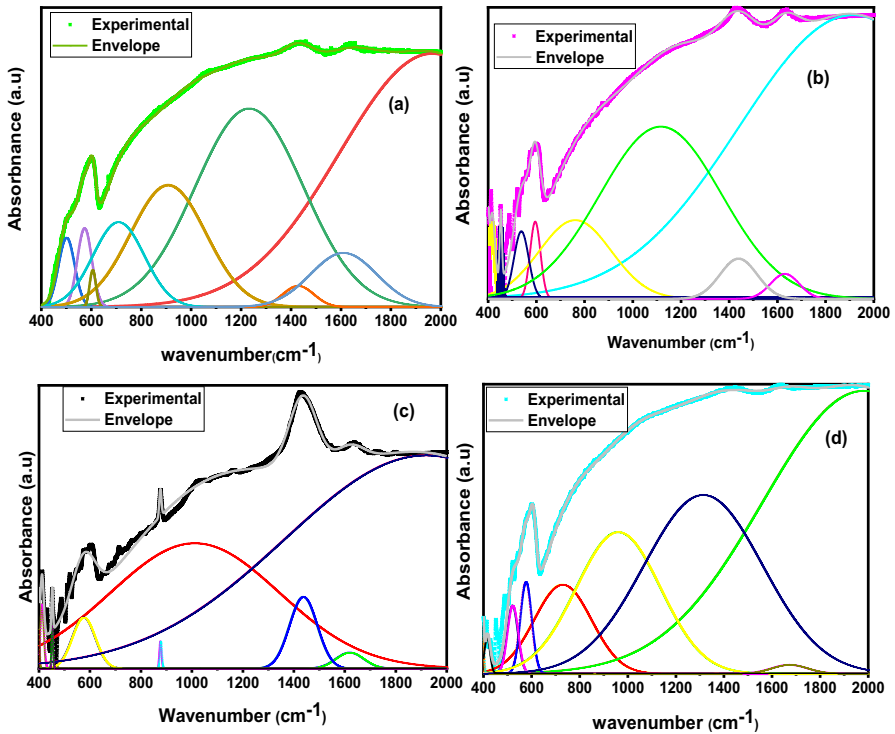


Fig. 4 FTIR absorbance spectra and deconvolution in the wave number range (400–2000 cm^{-1}) of CdMnO nanoparticles-added (Bi,Pb)-2212 samples, **a** pure, **b** 0.02 wt%, **c** 0.05 wt%, **d** 0.10 wt%. (Colour figure online)

Table 2 Effect of $(\text{Cd}_{0.95}\text{Mn}_{0.05}\text{O})_x$ addition on absorption bands positions in $\text{Bi}_{1.6}\text{Pb}_{0.4}\text{Sr}_{1.9}\text{Ca}_{1.1}\text{Cu}_{2.1}\text{O}_{8+\delta}$

Sample	Peak position (cm^{-1})					
	Cu–O	M–O	CaCO_3	SrCO_3	CO_3^{2-}	Bi-2212
Mn-0	458.609	591.024	707.44	928.28	1284.64	1660.56
Mn-1	525.092	593.112	734.503	952.703	1298.92	1640.168
Mn-2	537.48	598.133	759.875	1121.07	1436.003	1640.124
Mn-4	–	574.916	–	1028.538	1445.723	1626.905
Mn-5	521.463	575.040	734.325	967.073	1308.598	1675.716

bond (O–H) [34] while those at 2371 cm^{-1} are associated with the $\text{O}=\text{C}=\text{O}$ vibration [35]. The peak band at ($1626.9\text{--}1675.76\text{ cm}^{-1}$) is a characteristic of the Bi(Pb):2212 phase [37]. The appearance of the weak and broad absorption bands at 707.4 cm^{-1} and 1445.56 cm^{-1} may be due to the stretching vibration of

CO_3^{2-} [38], whereas the peaks at 928.28 and 458.69 cm^{-1} correspond to CaCO_3 and CuO absorption peaks, respectively [39, 40]. The absorption bands around 590 cm^{-1} correspond to metal oxide (M–O) vibration [13].

For the samples Mn-1 to Mn-4, the wave numbers of the absorption peaks experience a clear shift. A redshift for the bands corresponding to the Bi-2212 phase and a blueshift for the bands associated with the remaining functional groups. The intensity of the absorbance shows an increase with the addition of CdMnO .

It is believed that the variation of the lattice parameters and bond properties induced by the addition of CdMnO on the superconducting matrix, induces such shifts. Additionally, the deviations of the oxygen content and amount of charge carriers can also be accounted for by the deviations of the wave number position of the absorption bands [32, 41]. It was difficult to identify absorption bands associated with CdMnO due to its low concentration and because its peak is probably dominated by the peaks of metal oxides that fall in a close wave number range [15].

The variation of the DC-electrical resistivity versus temperature, for all samples, is graphically presented in Fig. 5. A normal state metallic-like behavior, followed by a superconducting transition is exhibited in all samples.

The electrical resistivity data, in the normal state, are well fitted to Matthiessen's rule [42]:

$$\rho = \rho_0 + \alpha T \quad (2)$$

where α is the resistivity temperature coefficient, and ρ_0 is the residual resistivity at 0 K. The fitting is shown for the pure sample in Fig. 5. The values of ρ_0 , α , and the room temperature resistivity $\rho_{300\text{K}}$ are listed in Table 3. The values of ρ_0 and $\rho_{300\text{K}}$ show a decrease with x . Studies have shown that ρ_0 is an indicator of the samples'

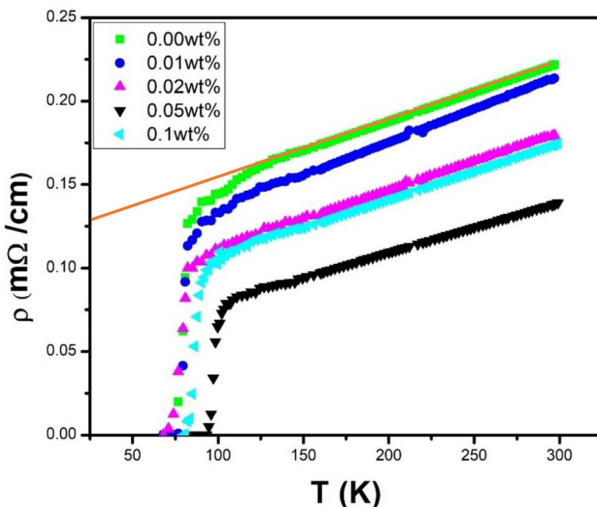


Fig. 5 Resistivity versus temperature plots of CdMnO nanoparticles doped (Bi,Pb)—2212 samples. (Colour figure online)

Table 3 Resistivity temperature coefficient α , residual resistivity at 0 K: ρ_0 , residual resistivity at 300 K: ρ_{300K} , superconducting transition temperature T_c , zero-resistivity temperature T_0 , superconducting transition width ΔT , index of transition γ , critical current density J_c , and flux pinning energy U for different CdMnO nanoparticle doped (Bi,Pb)-2212 samples

Mn (x)	ρ_0 (m Ω cm)	ρ_{300K} (m Ω cm)	$\alpha \times 10^{-4}$ (m Ω cm K $^{-1}$)	T_c (K)	T_0 (K)	ΔT_c (K)	P	J_c (A/cm 2)	γ	U (eV)
0.00	0.118	0.221	3.49	80.88	74	9.875	0.119	674.94	3.60	0.0233
0.01	0.094	0.213	4.00	83.62	79.5	4.125	0.121	688.93	3.62	0.0234
0.02	0.075	0.179	3.50	85.12	82.25	2.750	0.124	788.44	3.98	0.0257
0.05	0.073	0.174	3.40	87.78	86.39	1.390	0.126	822.34	4.13	0.0267
0.10	0.049	0.138	3.00	85.21	79.5	5.500	0.124	784.71	4.13	0.0267

purity [43], while ρ_{300K} is correlated with the number of scattering centers that arise due to oxygen vacancies and the disorder of cations [44]. The decrease in ρ_0 confirms the purity of the samples which is consistent with the XRD results, while the decrease in ρ_{300K} is attributed to the decrease of the grain boundaries resistance and defects due to CdMnO addition, which is also consistent with the SEM analysis. The values of α show slight variations with x , indicating that the addition of CdMnO had no significant effect on the charge carrier concentrations since they do not enter the crystal structure of the (Bi-Pb)2212 phase [45]

The Gaussian fitting of the temperature dependence of the $d\rho/dT$ curves allows us to determine the superconducting transition temperature (T_c), which corresponds to the maximum of the curve. The values of T_c , as well as the zero-resistivity temperature T_0 and the temperature width $\Delta T = T_c - T_0$ are also listed in Table 3.

The values of T_c and T_0 increase with the addition of CdMnO up to $x=0.05$ wt.%, and decrease for $x=0.1$ wt.%, while ΔT follows an inverse trend. The enhancement of T_c and T_0 might be attributed to the enhancement in the intergrain connectivity [46, 47] due to the addition of the CdMnO nanoparticles, whereas the diminishing of T_c for higher addition of CdMnO might be related to the increase in the oxygen content as determined for the Idiometric titration calculations and the breaking of the copper pairs due to the high concentration of CdMnO [48–50]. Furthermore, several studies have shown that the doping Mn doped CdO nanoparticles showed a shift in their magnetic signature from diamagnetic to ferromagnetic. The ferromagnetic behavior of CdMnO may cancel the supercurrents and terminate the Cu ion long-range coupling in the CuO layers. Similar behavior was observed by Basma et al. [51], for ferromagnetic CoFe_2O_4 addition on the Gd-123 system (Fig. 6).

Moreover, the superconducting properties of the Bi-2212 system are dependent on the hole concentration or the number of holes per Cu atom [52, 53]. A parabolic

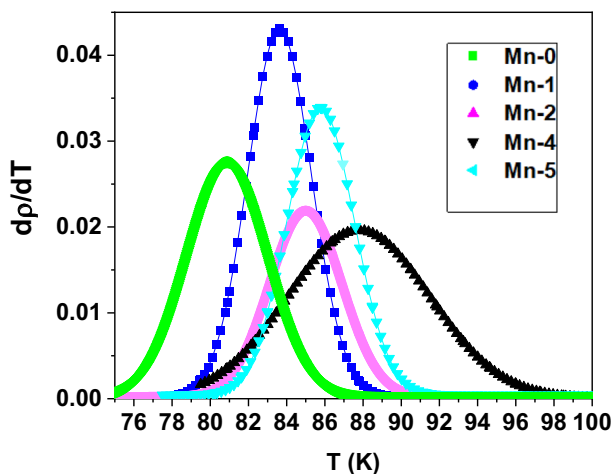


Fig. 6 $d\rho/dT$ versus Temperature plots of CdMnO nanoparticle doped (Bi,Pb)-2212 samples. (Colour figure online)

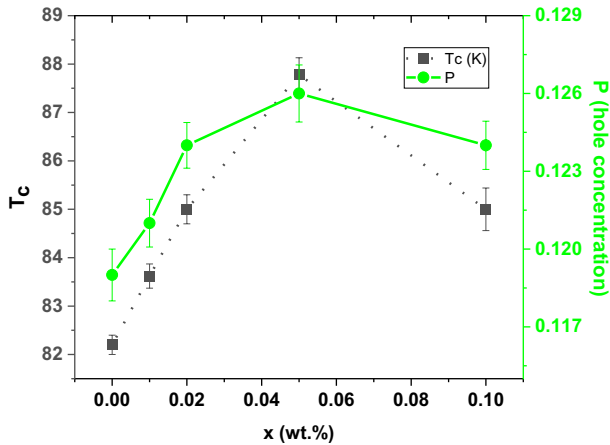


Fig. 7 The variation of T_c and hole concentration (P) versus the amount of added CdMnO for nanoparticle doped (Bi,Pb)-2212 samples. (Colour figure online)

relationship [54] holds between the superconducting transition temperature and the hole concentration as indicated in Eq. (3).

$$p = 0.16 - [(1 - T_c/T_{c \max})/82.6]^{1/2} \quad (3)$$

where p represents hole concentration and $T_{c \max}$ is taken as 85 K for the Bi-2212 system [55]. The values of P are listed in Table 3 while plots of P and T_c versus x are shown in Fig. 7. Both T_c and P increase with x up to 0.05. This increase might be due to the enhanced oxygen content that causes an excess of holes in the Cu-O₂ planes. Whereas, the decrease in the hole concentration for $x=0.1$ might be due to the distortions in lattice structure induced by the high additions of CdMnO [55].

The current–voltage characteristics are obtained at 70 K and are shown in terms of E and J , as depicted in Fig. 8a. The transport critical current density J_c , for all

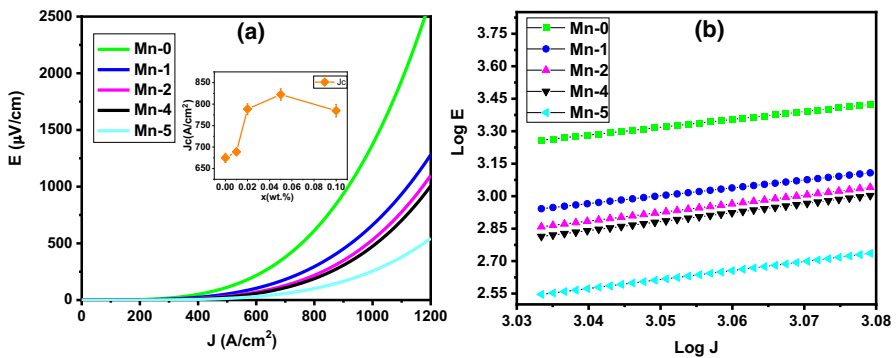


Fig. 8 **a** Variation of electric field as function of the critical current density for (CdMnO nanoparticles) doped (Bi,Pb)-2212 samples. **b** The logarithmic plots of E versus J . The inset of **a** represents the variation of J_c versus the CdMnO content. (Colour figure online)

samples, was measured using a criterion of $1 \mu\text{V}/\text{cm}$. The variation of J versus x is shown in the inset of Fig. 8a, and the values are presented in Table 3. J_c obeys a similar behavior to T_c , it demonstrates an improvement till $x=0.05$ followed by a reduction for the sample Mn-5. This enhancement in J_c may be ascribed to the development in grain connectivity. The increase in J_c may be attributed to the diffusion of CdMnO over the twin boundaries, pore surfaces, and grain boundaries. This can improve the flux pinning and coupling between grains, causing the increase of the critical current density. Similar results were reported for the Bi-2212 system added with Sm nanoparticles [56] and the Bi-2223 system added with Ag nanoparticles [7]. On the other hand, the reduction in J_c is ascribed to the excessive addition of CdMnO, which leads to large agglomerations between the grains and not through the boundaries and voids, which devastate the intergranular critical current density.

The form of the E – J characteristic of a superconductor can be demonstrated using the following equation

$$E = \alpha_j J^\gamma \quad (4)$$

where α_j , γ are material constants [57]. The γ -value characterizes the homogeneity of superconductors and is called the index of transition [58].

The logarithmic plots of E versus J as depicted in Fig. 8b, allows us to calculate γ , and the flux pinning energy U given by the relation: $\gamma=U/k_B T$ [59, 60]. The values of γ and U are listed in Table 3. The value of U increases with CdMnO addition to reach a maximum for $x=0.05\text{wt.}\%$ assuring the successful

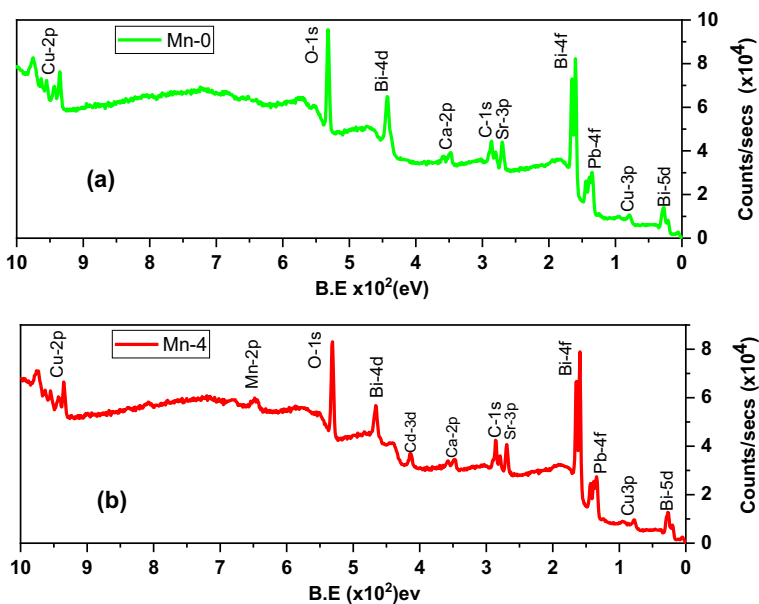


Fig. 9 XPS spectra of CdMnO nanoparticles-added (Bi,Pb)-2212 samples, **a** pure and **b** 0.05 wt.%. (Colour figure online)

incorporation of CdMnO nanoparticles as flux pinning centers at the level of grain boundaries.

The graphs of Fig. 9a and b demonstrate the XPS spectra of the samples Mn-0 and Mn-4. The survey spectra of the sample Mn-0 show the existence of Bismuth, Lead, Strontium, Calcium, copper, oxygen, and traces of Carbon. Moreover, the survey spectrum of the sample Mn-4 shows the presence of Cadmium and Manganese in addition to the above-mentioned elements. The presence of Carbon is attributed to the interaction of the sample with ambient air before the XPS measurement [61].

Furthermore, for a deeper investigation of the oxidation states of Bi, and Pb for both samples Mn-0 and Mn-4, Cu for the sample Mn-0 and Mn for the sample Mn-4, their main spectral lines are deconvoluted as shown in the high-resolution XPS spectra of Fig. 10.

The high-resolution XPS spectrum in Fig. 10a and b reveals the presence of two main peaks of Bi (Bi-4f) in Mn-0 and Mn-4 at 158.18 and 163.5 eV (Bi $4f_{7/2}$ and Bi $4f_{5/2}$). The Bi- $4f_{5/2}$ line is identical to the Bi_2O_3 spectra [62–64] and exhibits a +3 oxidation state of Bi. The deconvolution of the Bi- $4f_{7/2}$ and Bi- $4f_{5/2}$ spectra display the existence of a higher binding energy (HBE) constituent that may be ascribed to Bi⁵⁺ valency states [65] that arise from the substitution of Bi by Pb according to the Eq. (5) below:

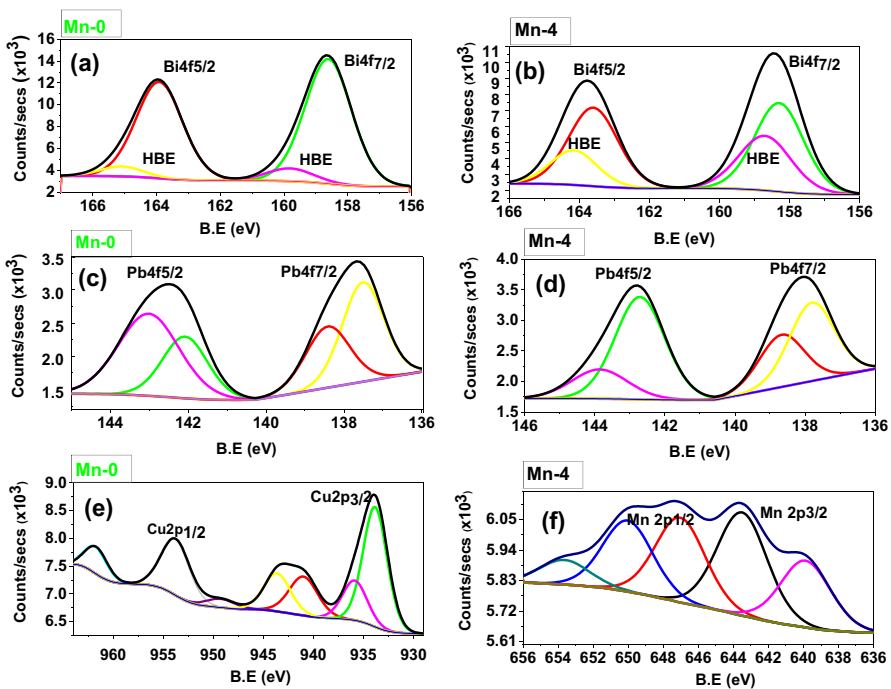
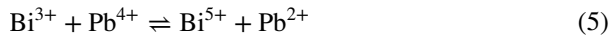


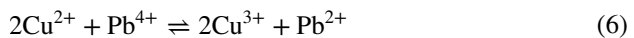
Fig. 10 The main spectral lines with deconvolution plots of Bi-4f, Pb-5f, Cu-2p, and Mn-2p for the pure and 0.05 wt.% samples. (Colour figure online)



The intensity of the HBE peak increases with CdMnO addition. The % contribution of Bi^{5+} increases from 22.21 to 35.48%. It is believed that the increase in the valency of Bi is due to the increase in the oxygen content near the Bi-O layers [66]. Moreover, the rise of the valence of Bi leads to an increase in the coulomb attraction in the BiO layer and hence can illustrate the reduction in the lattice parameter c as reported in Table 1. It was previously informed that when the Bi valency becomes larger than 3+, superconductivity is diminished [64, 65]. In fact, the increase in Bi valence causes the decrease of the number of electrons in the Bi-O planes. These are regarded as charge reservoirs for conduction. Consequently, the insulating Bi-O layers forbid the maintenance of superconducting phase coherence between the Cu-O planes. This might interpret the reduction in the superconducting transition temperature T_c for the higher addition of CdMnO nanoparticles (sample Mn-5) as a result of the high oxygen content.

Figure 10c, d shows the deconvoluted Pb-4f spectral lines of Mn-0 and Mn-4. The lines are composed of two components, ($4f_{7/2}$) and ($4f_{5/2}$). The deconvolution of the lines demonstrates a HBE component that might be ascribed to the presence of Pb in two different oxidation states, Pb^{2+} and Pb^{4+} [67]. A reduction in the Pb^{4+} contribution is due to the transformation of Pb^{4+} to Pb^{2+} according to the equilibrium reaction (6) shown below.

The Cu-2p XPS high-resolution spectrum is presented in Fig. 10e. The spectra show the spin-orbit split main lines $2P_{3/2}$ and $2P_{1/2}$ with their respective satellites at around 10 eV from each of them [68]. The main lines and their corresponding satellites demonstrate the d^9 and d^{10} final states. The evidence of the presence of Cu^{3+} valency (HBE component) is the deconvolution of the $2P_{3/2}$ line, which is critical to confirm neutrality and establishment of the (Bi-Pb)2212 superconductor [69]. In fact, the valency of the Cu ions is governed by the cationic equilibrium reaction stated in Eq. (6).



The improvement in superconductivity in the system is caused by the oxidation of Cu^{2+} to Cu^{3+} by increasing the hole carrier concentration [62, 70].

The XPS spectrum of Mn 2p is presented in Fig. 10(f). The successful addition of CdMnO is assured [71, 72]. The peak at 639.87 eV, correspond to MnO (Mn^{2+}) [73, 74], while the peak at 643.51 eV corresponds to Mn_2O_3 (Mn^{3+}) [75]. Moreover, the XPS spectra of Ca and Sr have demonstrated no significant variations with the addition of CdMnO nanoparticles.

It is believed that the superconductivity of the (Bi-Pb)-2212 is controlled by the electron transfer mechanism among Bi, Pb, and Cu as well as the changes of the oxygen content caused by the CdMnO addition. For the samples Mn-0, Mn-1, Mn-2, and Mn-4, the cationic exchange occurs according to Eq. (6), and then the number of hole carriers is improved and hence the superconductivity is improved. For Mn-5, the high oxygen content favors the variation of the valency of Bi^{3+} to Bi^{5+} according to Eq. (5), and the superconductivity deteriorates for the high valency of Bi^{3+} as explained above.

4 Conclusion

(CdMnO) nanoparticles (Bi,Pb)-2212 phase ($x=0.00, 0.01, 0.02, 0.05,$ and 0.1 wt.%) superconducting samples have been prepared by the conventional solid-state reaction technique. XRD analysis assures phase purity and crystallinity. The lattice parameters are changed due to the distortion induced in the BiO layers and Cu–O bonding caused by the increase of the oxygen content, as measured through Idiometric titration analysis. SEM images demonstrate an improvement in the structure and morphology of the sample as a result of CdMnO addition. FTIR spectroscopy suggests that the addition of CdMnO was clear through the shift of the absorption bands. Dc-electrical resistivity measurements and I – V characteristics, respectively, have demonstrated an enhancement of the superconducting transition temperature (T_c) and the critical current density (J_c) with CdMnO addition up to $x=0.05$ wt %. A similar variation trend was presented for the flux pinning potential. The successful incorporation of the added CdMnO nanoparticles leads to the improvement in the superconducting parameters at the level of grain boundaries which improves the intergrain linkage and acts as impressive magnetic flux pinning centers. However, for higher additions of CdMnO, the ferromagnetic contribution deteriorates the superconductivity. Moreover, the XPS studies exhibit that the superconductivity of the (Bi-Pb)-2212 is controlled by the electron transfer mechanism among Bi, Pb, and Cu as well as the variations of the oxygen content prompted by the CdMnO addition.

Acknowledgements This research was accomplished in the Specialized Materials Science Lab and Advanced Nanomaterials Research Lab, Physics Department, Faculty of Science, Beirut Arab University, Lebanon in collaboration with the superconductivity and metallic-glass lab, Faculty of Science, Alexandria University, EGYPT. The authors acknowledge Mr. Wafic Labban for his assistance in sample preparation.

Funding This research did not receive any specific grant from funding agencies in the public, commercial, or not-for-profit sectors.

References

1. A.T. Ulgen, G. Yildirim, J. Mater. Sci. Mater. Electron **30**, 8268–8277 (2019)
2. M.J. Masnita, R. Abd-Shukor, Results Phys. **17**, 103177 (2020)
3. A.T. Ulgen, T. Turgay, C. Terzioglu, G. Yildirim, M. Oz, J. Alloy. Compd **764**, 755–766 (2018)
4. W. Labban, W. Malaeb, K. Habanjar, M.S. Hassan, R. Sakagami, Y. Kamihara, R. Awad, Ph. Trans. **93**, 1055–66 (2020)
5. S.B. Guner, Y. Zalaoglu, T. Turgay, O. Ozyurt, A.T. Ulgen, M. Dogruer, G. Yildirim, J. Alloy. Compd. **772**, 388–398 (2019)
6. K. Belala, A. Galluzzi, M.F. Mosbah, M. Polichetti, Mater. Sci. Pol. **39**, 15–23 (2021)
7. M.Q. Al Habeeb, S. Oboudi, W. Wenlong, S. Julian, J. Phys. Conf. Ser. **1829**, 012024 (2021)
8. S.F. Nasution, S. Humaidi, A. Imaduddin, N. Darsono, H. Nugraha, J. Phys. Conf. Ser. **1882**, 012021 (2021)
9. S.E.M. Ghahfarokhi, N. Hoseenzadeh, M.Z. Shoushtari, J. Supercond. Nov. Magn. **27**, 2217–2223 (2014)
10. N.A.A. Yahya, R Al-Gaashani and RA bd-Shukor. Appl. Phys. A **123**, 168 (2017)

11. H. Gündoğmuş, J. Mater. Sci. Mater. Electron. **28**, 12598–12605 (2017)
12. J. Zhang, W. Wang, T. Wang, L. Jiang, N. Wang, D. Sun, X. Zhao, M. Wang, Y. Qi, J. Alloy. Compd. **858**, 157650 (2021)
13. A. Sedky, A. Salah, J. Low. Temp. Phys. **201**, 294–310 (2020)
14. C. Bhukkal, R. Ahlawat, Res. Chem. Intermed. **46**, 4211–4232 (2020)
15. A.A. Dakhel, J. Supercond. Nov. Magn. **33**, 1871–1877 (2020)
16. B.R. Kumar, K.H. Prasad, K. Kasirajan, M. Karunakaran, V. Ganesh, Y. Bitla, S. AlFaify, I.S. Yahia, Sens. Actuator A Phys. **319**, 112544 (2021)
17. S. Abbas, H. Basma, Al.J.R. Boukhari, Awad. Appl. Phys. A **127**, 505 (2021)
18. P Christuraj M Dinesh Raja S Pari G Satheesh kumar and V Uma Shankar 2020 *Mater. Today: Proc*
19. S. Dugan, M.M. Koç, B. Coşkun, J. Mol. Struct. **1202**, 127235 (2020)
20. K. Kasirajan, A.N.A. Anasthasiya, O.M. Aldossary, M. Ubaidullah, M. Karunakaran, Sens. Actuator A Phys. **319**, 112531 (2021)
21. R. Cabassi, D. Delmonte, M.M. Abbas, A.R. Abdulridha, E. Gilioli, Crystals **10**, 462 (2020)
22. S. Vinu, P.M. Sarun, A. Biju, R. Shabna, PG uruswamy and U Syamaprasad. Supercond. Sci. Technol. **21**, 045001 (2008)
23. L. Lutterotti Maud, Acta Cryst A **56**, 54–54 (2000)
24. S. Pallian Murikoli, A. Biju, P. Guruswamy, S. Upendran, J. Am. Ceram. Soc. **90**, 3138–41 (2007)
25. H. Baqiah, S.A. Halim, S.K. Chen, K.P. Lim, M.M. Awang Kechik, Sains Malays **45**, 643–519 (2016)
26. X. Sun, X. Zhao, W. Wu, X. Fan, X.-G. Li, H.C. Ku, Physica. C Supercond. **307**, 67–73 (1998)
27. M. Yilmazlar, H.A. Cetinkara, M. Nursoy, O. Ozturk, C. Terzioglu, Physica. C Supercond. **442**, 101–107 (2006)
28. S.M. Khalil, AIP Adv. **2**, 042183 (2012)
29. A. Sedky, W. Al-Battat, Phys. B Condens. Matter **410**, 227–232 (2013)
30. D.C. Harris, M.E. Hills, T.A. Hewston, J. Chem. Educ. **64**, 847 (1987)
31. W.M. Chen, X.S. Wu, J.F. Geng, J. Chen, D.B. Chen, X. Jin, S.S. Jiang, J. Supercond. **10**, 41–44 (1997)
32. J. Hwang, T. Timusk, G.D. Gu, Nature **427**, 714–717 (2004)
33. F. Jean, G. Collin, M. Andrieux, N. Blanchard, J.-F. Marucco, C Supercond. **339**, 269–80 (2000)
34. M.R. Norman, H. Ding, M. Randeria, J.C. Campuzano, T. Yokoya, T. Takeuchi, T. Takahashi, T. Mochiku, K. Kadowaki, P. Guptasarma, D.G. Hinks, Nature **392**, 157–160 (1998)
35. J.W. Alldredge, J. Lee, K. McElroy, M. Wang, K. Fujita, Y. Kohsaka, C. Taylor, H. Eisaki, S. Uchida, P.J. Hirschfeld, J.C. Davis, Nat. Phys. **4**, 319–326 (2008)
36. T. Anantha Kumar, S.C.V.M. MalathiMythilijeyachandran, IJCTR **11**, 48–57 (2018)
37. C.B. Alcock, B. Li, J. Am. Ceram. Soc. **73**, 1176–1180 (1990)
38. E. Alibakhshi, E. Ghasemi, M. Mahdavian, B. Ramezanzadeh, Prog. Color. Color. Coat. **9**(4), 233–248 (2016)
39. A.H. Qureshi, M. Arshad, K. Masud, A. Saeed, J. Therm. Anal. Calorim. **81**, 363–367 (2005)
40. N. Arshad, M. Arshad, F.R. Sale, A.H. Qureshi, S.K. Durrani, S.U. Rehman, JCSP **25**, 177 (2011)
41. R. Kumar, H.S. Singh, Y. Singh, AIP Conf. Proc. **1953**, 030001 (2018)
42. A.E. White, R.C. Dynes, J.P. Garno, Phys. Rev. B **33**, 3549–3552 (1986)
43. H. AbuHlaiwa, H. Basma, M. Rekaby, M. Roumie, R. Awad, J. Low Temp. Phys. **198**, 26–40 (2020)
44. C. Mao, L. Zhou, X. Wu, X. Sun, Supercond. Sci. Technol. **9**, 994–1000 (1996)
45. R. Awad, M. Roumie, S. Isber, S. Marhaba, A.I. AbouAly, H. Basma, J Supercond. Nov. Magn. **28**, 535–539 (2015)
46. A. Tampieri, G. Celotti, S. Lesca, G. Bezzi, T.M.G. La Torretta, G. Magnani, J. Eur. Ceram. Soc. **20**, 119–126 (2000)
47. E. Brecht, W.W. Schmahl, G. Miehe, M. Rodewald, H. Fuess, N.H. Andersen, J. Hanßmann, Th. Wolf, Physica C Superconduct **265**, 53–66 (1996)
48. A. Mellekh, M. Zouaoui, F. Ben Azzouz, M. Annabi, M. Ben Salem, Solid State Commun. **140**, 318–323 (2006)
49. H.K. Barik, S.K. Ghorai, S. Bhattacharya, D. Kilian, B.K. Chaudhuri, J. Mater. Res. **15**, 1076–1082 (2000)
50. H Basma R Awad M Roumie S Isber S Marhaba A Abou-Aly 2016J *Supercond Nov Magn* **29**
51. H. Basma, M. Roumie, R. Awad, S. Marhaba, M. Albast, A. Abualy, Mater. Sci. Appl. **06**, 828 (2014)
52. O. Bilgili, K. Kocabaş, J. Mater. Sci. Mater. Electron **26**, 1700–1708 (2015)

53. M.B. Maple, J. Magn. Magn. Mater. **177–181**, 18–30 (1998)
54. O. Bilgili, Y. Selamet, K. Kocabaş, J. Supercond. Nov. Magn. **21**, 439–449 (2008)
55. Y. He, M. Hashimoto, D. Song, S.-D. Chen, J. He, I.M. Vishik, B. Moritz, D.-H. Lee, N. Nagaosa, J. Zaanen, T.P. Devereaux, Y. Yoshida, H. Eisaki, D.H. Lu, Z.-X. Shen, Science **362**, 62–65 (2018)
56. M. Mimouni, M.S. Mahboub, N. Mahamdioua, M.F. Mosbah, G. Rihia, S. Zeroual, M. Ghougali, S.P. Altintas, A. Alhoussein, J. Supercond. Nov. Magn. **33**, 3321–3331 (2020)
57. R. Awad, A.I. Abou Aly, N.H. Mohammed, S. Isber, H.A. Motaweh, D. El-Said Bakeer, J. Alloy. Compound. **610**, 614–622 (2014)
58. I. Falorio, E.A. Young, Y. Yang, J. Phys. Conf. Ser. **507**, 022004 (2014)
59. B. Ni, T. Wakuda, K. Funaki, IEEE Trans. Appl. Supercond. **7**, 2118–2121 (1997)
60. F. Vallès, A. Palau, V. Rouco, B. Mundet, X. Obradors, T. Puig, Sci. Rep. **8**, 5924 (2018)
61. A. Khalid, P. Ahmad, A.I. Alharthi, S. Muhammad, M.U. Khandaker, M.R.I. Faruque, A. Khan, I.U. Din, M.A. Alotaibi, K. Alzimami, A.A. Alfuraih, D.A. Bradley, Material **14**, 3223 (2021)
62. V. Gayathri, E.P. Santanu Bera, T.G. Amaladass, R.P. Kumary, Awadhesh Mani, Phys. Chem. Chem. Phys. **23**(22), 12822 (2021)
63. H. Chen, Y. Li, M. Wang, G. Han, M. Shi, X. Zhao, J. Supercond. Nov. Magn. **33**, 3015–3025 (2020)
64. B.R. Sekhar, N.L. Saini, P. Srivastava, K.B. Garg, J. Phys. Chem. Solids **55**, 49–58 (1994)
65. D.K. Rai, Asok K. Sarkar, T.N. Wittberg, Binod Kumar, J. Appl. Phys. **66**(8), 3950–3952 (1989)
66. Y. Idemoto, S. Ichikawa, K. Fueki, Physica C Supercond. **181**, 171–178 (1991)
67. S. Kambe, Y. Murakoshi, R. Sekine, M. Kawai, K. Yamada, S. Ohshima, K. Okuyama, Phys. C: Supercond. **190**, 139–140 (1991)
68. K. Watanabe, Supercond. Sci. Technol. **11**, 843–851 (1998)
69. X. Ma, Q. Hao, G. Liu, H. Zheng, X. Xu, G. Jiao, S. Zhang, C. Li, P. Zhang, Mater. Lett. **162**, 5–8 (2016)
70. A. Sedky, A. Salah, A. Abou-Aly, J. Supercond Nov Magn **33**, 3349–3359 (2020)
71. A.F. Carley, M.W. Roberts, J.S. Lees, R.J.D. Tilley, J. Chem. Soc. Faraday Trans. **86**, 3129–3134 (1990)
72. Z. Yan, L. Du, D.L. Phillips, RSC Adv. **7**, 55993–55999 (2017)
73. S. Richards, M.A. Baker, M.D. Wilson, A. Lohstroh, P. Seller, Opt. Lasers Eng. **83**, 116–125 (2016)
74. J.S. Hammond, S.W. Gaarenstroom, N. Winograd, Anal. Chem. **47**, 2193–2199 (1975)
75. S. Ciampi, V. Di Castro, C. Furlani, G. Polzonetti, J. Electron Spectrosc. Relat. Phenom. **60**, 375–383 (1992)

Publisher's Note Springer Nature remains neutral with regard to jurisdictional claims in published maps and institutional affiliations.